CrossMark

Active zinc-blende III–nitride photonic structures on silicon

Sylvain Sergent[1], Satoshi Kako[2], Matthias Bürger[3], Sarah Blumenthal[3],
Satoshi Iwamoto[1,2], Donat Josef As[3], and Yasuhiko Arakawa[1,2]

[1]Institute for Nano Quantum Information Electronics, The University of Tokyo, Meguro, Tokyo 153-8505, Japan
[2]Institute of Industrial Science, The University of Tokyo, Meguro, Tokyo 153-8505, Japan
[3]Universität Paderborn, Department Physik, 33095 Paderborn, Germany

We use a layer transfer method to fabricate free-standing photonic structures in a zinc-blende AlN epilayer grown by plasma-assisted molecular beam epitaxy on a 3C-SiC pseudosubstrate and containing GaN quantum dots. The method leads to the successful realization of microdisks, nanobeam photonic crystal cavities, and waveguides integrated on silicon (100) and operating at short wavelengths. We assess the quality of such photonic elements by micro-photoluminescence spectroscopy in the visible and ultraviolet ranges, and extract the absorption coefficient of ZB AlN membranes ($\alpha \sim (2\text{–}5) \times 10^2\,\mathrm{cm^{-1}}$). © 2016 The Japan Society of Applied Physics

Group-III nitrides are currently the dominant material system for conventional short-wavelength semiconductor light sources: from deep ultraviolet (UV) light-emitting diodes to visible light-emitting diodes and laser diodes. Because of the possibility of tailoring large band offsets and large exciton binding energies in III–nitride quantum dots (QDs), such materials have great potential for the realization of novel active nanophotonic devices operating at high temperatures such as single-photon sources.[1,2] For future practical applications and large-scale integration, it is crucial not only to integrate such active heterostructures on silicon but also to couple them with photonic elements (waveguides, microdisks, and photonic crystals) realized in the same semiconductor system. This would lead to all-III–nitride on-chip nanophotonics integrated on silicon and operating at high temperatures. Most of the group-III nitride nanophotonic elements investigated so far dealt with wurtzite phase or polycrystalline structures: waveguides,[3–5] microdisks,[6–8] and even one-dimensional (1D)[9–12] and two-dimensional (2D)[3,4,13–17] photonic crystal nanocavities have already been reported in such systems. On the other hand, owing to the difficulty in processing the 3C-SiC pseudosubstrate, only microdisk cavities have been reported so far in the zinc-blende phase of group-III nitrides.[18] The nonpolar zinc-blende (ZB) phase of group-III nitrides is, however, an attractive structure, as it allows active heterostructures with large oscillator strengths[19,20] and high-temperature operation[21,22] to be achieved.

In this Letter, we report on the realization of various free-standing ZB AlN photonic structures containing GaN QDs in the frame of a layer transfer method:[11] waveguides, microdisks, and photonic crystal nanocavities. The quality of the photonic elements is probed by microphotoluminescence (μPL), using the emission of the QD ensemble. We report that the quality factors are as high as 530 in microdisk and photonic crystal nanocavities, and that the measured losses are 67 dB/mm in waveguide structures operating in the near-UV range.

The samples are grown on a 3C-SiC pseudosubstrate by plasma-assisted molecular beam epitaxy, according to the process described in Ref. 23. A 35-nm-thick ZB AlN buffer layer is first deposited on the pseudosubstrate and self-assembled ZB GaN QDs are subsequently grown by the Stranski–Krastanov technique, leading to a high QD density ($>10^{11}\,\mathrm{cm^{-2}}$). They are finally capped by a 35 nm ZB
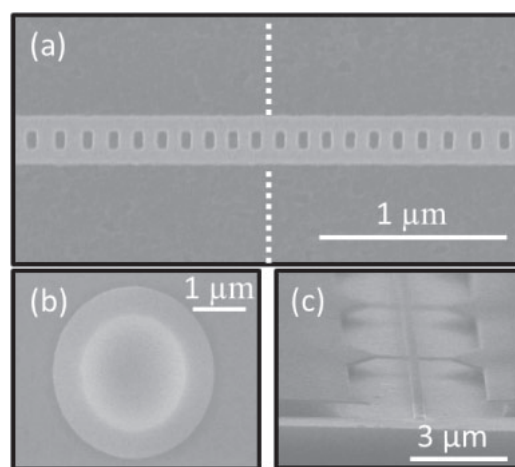

Fig. 1. Scanning electron microscopy images of (a) a nanobeam photonic crystal cavity, (b) a microdisk, and (c) a waveguide obtained from the transfer of a ZB AlN epilayer to a Si(001) host substrate. The dashed line in (a) highlights the center of the nanobeam cavity.

AlN layer. The QD plane is positioned at the center of the epilayer. Similarly to Ref. 11, the epilayer is transferred to a Si(001) substrate by bonding and subsequent back-etching of the 3C-SiC pseudosubstrate. Because the pseudo-substrate is composed of a 15-μm-thick 3C-SiC layer on a 500 μm Si(100) substrate, we perform SF6-based inductively coupled plasma reactive ion etching in two steps: the silicon is first removed by a 300 V bias-voltage plasma at a rate of 4 μm/min and then the remaining 3C-SiC is slowly etched with no bias voltage at a rate of 10 μm/h. The photonic structures are then defined by electron beam lithography and development of a ZEP520 positive resist for waveguides and photonic crystal cavities and a FOx15 negative resist for microdisks. The patterns are transferred in the III–nitride epilayer by Cl₂/Ar ion-coupled plasma reactive ion etching. The photonic structures are finally released by HF etching of the underlying hydrogen silsesquioxane layer that was used as a bonding layer. Scanning electron microscopy images of the three kinds of photonic structure are shown in Fig. 1. Similarly to Ref. 12, the 1D photonic crystal nanobeam is designed as an array of rectangular air holes with the period $a = 140\,\mathrm{nm}$ in a free-standing ridge waveguide with the width $w = 2a$. The array is tapered towards its center, forming the optical nanocavity: the taper follows the interpolation

$a_k^{-1} - a_0^{-1} \propto k^2$, where $k = 0, 1, \ldots, N - 1$ is the hole index, $a_0 = 0.84a$ is the hole pitch at the center of the cavity, and $2N = 16$ is the number of holes constituting the taper. The microdisk diameter is varied between 1 and 5 µm. The waveguide width is 300 nm and it is supported by 50-nm-wide tethers positioned on both sides of the guide every 10 µm.

The photonic structures are probed by µPL, using the emission of the embedded GaN/AlN QDs. The samples are inserted in a He-cooled cryostat at 4 K. The QDs are excited by a continuous-wave laser emitting at 266 nm through a Mitutoyo UV microscope objective with a 0.4 numerical aperture and a 50-fold magnification and oriented orthogonally to the sample surface. The resulting excitation spot diameter is about 2 µm. The microdisk cavity signal is measured both in confocal and orthogonal geometries. In the former case, the QD µPL signal is collected from the excitation objective, propagates in free space, and is dispersed by a 150 or 600 grooves/mm grating on a high-density charge-coupled device camera. In the latter case, the signal is collected by a Mitutoyo near-UV microscope objective that is placed in the microdisk plane and has a 0.4 numerical aperture and a 20-fold magnification, and is focused at the excitation point. It is then coupled to a multimode fiber by a Thorlabs UV-B objective with a 0.13 numerical aperture and a 5-fold magnification. The fiber output signal is finally dispersed by the grating on the charge-coupled device camera. In orthogonal geometry, and unlike previously reported ZB AlN microdisks,[18] our microdisk cavities exhibit periodically spaced whispering-gallery mode resonances in the visible and near-UV ranges, whereas control square mesas of similar dimensions do not exhibit any resonant peaks (Fig. 2). As expected from whispering-gallery modes,[24] µPL spectra do not show any resonance in confocal geometry (not shown here), which confirms the good structural quality of the microdisks. The spectral positions of the resonances agree well with the calculations obtained in the frame of the whispering-gallery mode approximation; thus, we can attribute a $TE_{m,n}$ mode to each resonance with m the azimuthal number and n the radial number (Fig. 2). The maximum quality factor is $Q_{exp} = 5 \times 10^2$ for the $TE_{26,1}$ mode propagating at $\lambda = 395$ nm in a 2 µm microdisk. It is far from the intrinsic quality factor of such whispering-gallery modes $Q_{int} > 10^9$, with Q_{int} calculated as[25]

$$Q_{int} = \exp\left[2m\left(\tanh^{-1}\left(\sqrt{1 - \frac{1}{n_{eff}^2}}\right) - \sqrt{1 - \frac{1}{n_{eff}^2}}\right)\right],$$

where $n_{eff} = 1.7$. Q_{exp} turns outs to be more than one order of magnitude lower than that previously reported for wurtzite AlN microdisks, presenting a similar level of fabrication disorder[7] and expected to present scattering losses of the same order of magnitude. Moreover, we observe no dependence of Q_{exp} on the microdisk diameter; thus, Q_{exp} should not be limited by scattering losses.[26] This suggests that the quality factor is mainly limited by absorption losses $Q_{abs}^{-1} = \alpha\lambda/2\pi n_{eff}$, which leads to an absorption coefficient α of $\sim 5 \times 10^2$ cm^{-1}. The absorption of GaN QDs is low owing to their discrete density of states; thus, the main source of absorption should come from crystal disorder in the ZB AlN barriers and GaN QD wetting layer: states related to point defects, heterogeneous strain, impurities, and wurtzite phase inclusions would all contribute to a high absorption tail of the
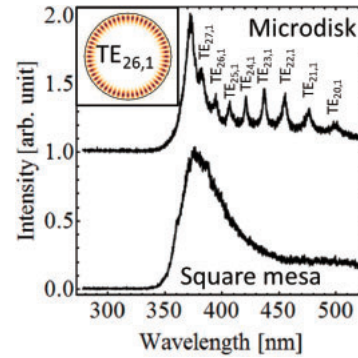

Fig. 2. Normalized side-collection µPL spectra of a 2 µm microdisk and a 5 µm square mesa. The spectra are offset along the vertical axis for clarity. The microdisk presents resonant modes with quality factors as high as 5×10^2 in the visible range. From the calculation of the whispering-gallery mode wavelength, we attribute each resonance to a mode $TE_{m,n}$ with m the azimuthal number and n the radial number. The inset shows the intensity of the cavity mode $TE_{26,1}$ as calculated in the frame of the whispering-gallery approximation.

barriers and wetting layer. The presence of such states is confirmed by the intense visible band that allows us to probe the whispering-gallery modes below the ZB GaN bandgap. Let us note that the crystal disorder of our QD samples has been observed through the mesoscopic PL of ZB GaN QDs[27] and has been shown to be greater in antiphase domains oriented along ZB AlN[110]. It is worth noting that in wurtzite AlN microdisks, the high crystal quality does not lead to an absorption tail limiting the quality factor at such wavelengths, but in wurtzite $Al_{0.5}Ga_{0.5}N$ microdisks embedding GaN QDs, the quality factor is also degraded by the barrier absorption tail.[7]

The nanobeam cavities are characterized in confocal geometry. The nanobeam cavity µPL spectra exhibit three resonances in the near-UV range [Fig. 3(a)], in agreement with the fundamental, first-order, and second-order TE-like modes obtained from three-dimensional finite-difference time-domain calculations [Fig. 3(c)]. Despite a good structural quality and high intrinsic quality factors $Q_{int} > 10^5$, the highest experimental quality factor obtained is $Q_{exp} = 5.3 \times 10^2$ at $\lambda = 395$ nm [Fig. 3(b)]. This is more than an order of magnitude lower than what has been reported for wurtzite AlN nanobeam cavities,[12] and is in good agreement with the microdisk quality factors reported in the present work: once again the absorption tail of the AlN barriers and GaN QD wetting layer limits the nanobeam cavity performance.

For the waveguide structures, the QD signal is collected in confocal and orthogonal geometries but, as opposed to microdisk cavities, the QDs are excited at different positions of the waveguide and the side-collection objective is focused on the waveguide output. Figure 4 shows the integrated intensity of the side-collected QD µPL signal between 350 and 400 nm normalized by the signal collected from the top objective. As the light propagates along the waveguide, the waveguide output intensity decreases significantly: exponential fitting to the data shows that losses are as high as $\alpha \sim 67$ dB/mm ($\sim 2 \times 10^2$ cm^{-1}). This value is actually lower than that extracted from the microdisk quality factor. This result cannot be explained by the difference in modal loss for the microdisk and waveguide structures since the calculated confinement factors turn out to be similar in both structures.
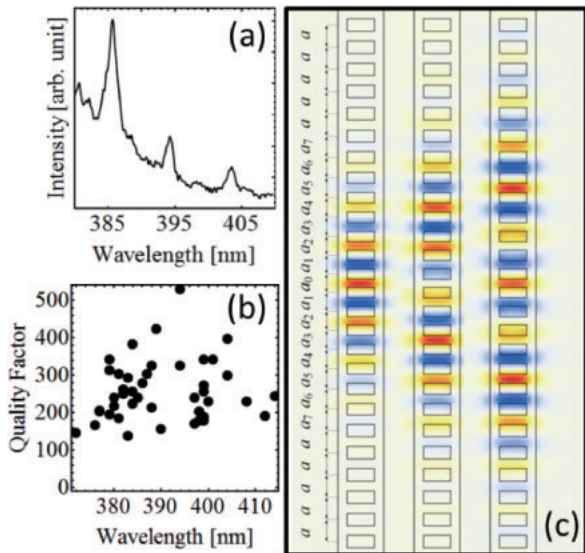
Fig. 3. (a) Confocal-geometry µPL spectrum of a free-standing ZB AlN nanobeam cavity. (b) Quality factor of nanocavity modes measured by µPL for nanobeams presenting air hole sizes along the nanobeam axis ranging from r = 0.22a to 0.28a. (c) Three-dimensional finite-difference time-domain calculations of the fundamental, first-order, and second-order cavity TE-like modes superimposed to the cavity design.
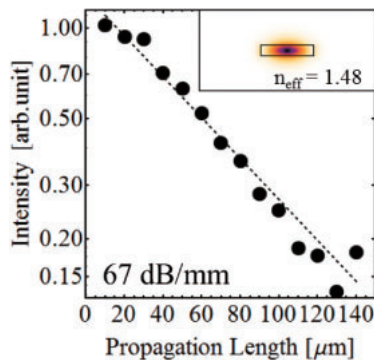

Fig. 4. Integrated intensity of the side-collection µPL spectra of a single-mode ZB AlN waveguide surrounded by air between $\lambda = 350$ and $400\,\text{nm}$. The vertical axis is in log scale. The intensities are measured for different excitation points along the waveguide, which define the propagation length. The intensities are normalized by the intensity collected in confocal geometry at each excitation point. The inset represents the finite element calculation of the waveguide single TE mode intensity with the effective index of 1.48 at $\lambda = 380\,\text{nm}$.

This might be due to the collection of light that is not guided in the waveguide but rather scattered by the tethers. In any case, losses are significantly higher than those found in waveguides operating at long wavelengths,[3,5] as absorption and scattering have a larger impact in the UV range. However, polycrystalline AlN waveguides present very similar losses ($\alpha \sim 65\,\text{dB/mm}$ at $\lambda = 400\,\text{nm}$)[5] and thus do not outperform ZB AlN because the polycrystalline material also suffers from a large absorption at short wavelengths.

In conclusion, we have demonstrated the versatility of the layer transfer method to fabricate a large variety of ZB III–nitride photonic structures operating at short wavelengths, including photonic crystal nanocavities and waveguides that were yet to be reported for ZB III–nitrides. In the considered wavelength range, the photonic structures are shown to be mainly limited by the absorption α of $\sim(2–5.0) \times 10^2\,\text{cm}^{-1}$ of

the AlN barrier and GaN QD wetting layer. An enhancement of the photonic structure performance would thus require improving the crystalline quality of the ZB epitaxial layer. Such improvement would lead to higher quality factors of cavity resonances and would open the way to nanolasing or cavity quantum electrodynamics effects in ZB nitrides.

1) S. Kako, C. Santori, K. Hoshino, S. Gotzinger, Y. Yamamoto, and Y. Arakawa, Nat. Mater. **5**, 887 (2006).
2) M. J. Holmes, K. Choi, S. Kako, M. Arita, and Y. Arakawa, Nano Lett. **14**, 982 (2014).
3) U. Dharanipathy, N. Vico Triviño, C. Yan, Z. Diao, J.-F. Carlin, N. Grandjean, and R. Houdré, Opt. Lett. **37**, 4588 (2012).
4) N. Vico Triviño, U. Dharanipathy, J.-F. Carlin, Z. Diao, R. Houdré, and N. Grandjean, Appl. Phys. Lett. **102**, 081120 (2013).
5) M. Stegmaier, J. Ebert, J. M. Meckbach, K. Ilin, M. Siegel, and W. H. P. Pernice, Appl. Phys. Lett. **104**, 091108 (2014).
6) D. Simeonov, E. Feltin, H.-J. Bülhmann, T. Zhu, A. Castiglia, M. Mosca, J.-F. Carlin, R. Butté, and N. Grandjean, Appl. Phys. Lett. **100**, 071103 (2012).
7) M. Mexis, S. Sergent, T. Guillet, C. Brimont, T. Bretagnon, B. Gil, F. Semond, M. Leroux, D. Néel, S. David, X. Chécoury, and P. Boucaud, Opt. Lett. **36**, 2203 (2011).
8) I. Aharonovich, A. Woolf, K. J. Russell, T. Zhu, N. Niu, M. J. Kappers, R. A. Oliver, and E. L. Hu, Appl. Phys. Lett. **103**, 021112 (2013).
9) W. H. P. Pernice, C. Xiong, C. Schuck, and H. X. Tang, Appl. Phys. Lett. **100**, 091105 (2012).
10) S. Sergent, M. Arita, S. Kako, S. Iwamoto, and Y. Arakawa, Appl. Phys. Lett. **100**, 121103 (2012).
11) S. Sergent, M. Arita, S. Kako, K. Tanabe, S. Iwamoto, and Y. Arakawa, Appl. Phys. Lett. **101**, 101106 (2012).
12) S. Sergent, M. Arita, S. Kako, K. Tanabe, S. Iwamoto, and Y. Arakawa, Phys. Status Solidi C **10**, 1517 (2013).
13) M. Arita, S. Ishida, S. Kako, S. Iwamoto, and Y. Arakawa, Appl. Phys. Lett. **91**, 051106 (2007).
14) D. Néel, S. Sergent, M. Mexis, D. Sam-Giao, T. Guillet, C. Brimont, T. Bretagnon, F. Semond, B. Gayral, S. David, X. Checoury, and P. Boucaud, Appl. Phys. Lett. **98**, 261106 (2011).
15) N. Vico Triviño, G. Rossbach, U. Dharanipathy, J. Levrat, A. Castiglia, J.-F. Carlin, K. A. Atlasov, R. Butté, R. Houdré, and N. Grandjean, Appl. Phys. Lett. **100**, 071103 (2012).
16) D. Sam-Giao, D. Néel, S. Sergent, B. Gayral, M. J. Rashid, F. Semond, J. Y. Duboz, M. Mexis, T. Guillet, C. Brimont, S. David, X. Checoury, and P. Boucaud, Appl. Phys. Lett. **100**, 191104 (2012).
17) M. Arita, S. Kako, S. Iwamoto, and Y. Arakawa, Appl. Phys. Express **5**, 126502 (2012).
18) M. Bürger, G. Callsen, T. Kure, A. Hoffmann, A. Pawlis, D. Reuter, and D. J. As, Appl. Phys. Lett. **103**, 021107 (2013).
19) J. Simon, N. Pelekanos, C. Adelmann, E. Martinez-Guerrero, R. André, B. Daudin, L. S. Dang, and H. Mariette, Phys. Rev. B **68**, 035312 (2003).
20) S. Sergent, S. Kako, M. Bürger, D. J. As, and Y. Arakawa, Appl. Phys. Lett. **103**, 151109 (2013).
21) S. Kako, M. Holmes, S. Sergent, M. Bürger, D. J. As, and Y. Arakawa, Appl. Phys. Lett. **104**, 011101 (2014).
22) S. Sergent, S. Kako, M. Bürger, T. Schupp, D. J. As, and Y. Arakawa, Appl. Phys. Lett. **105**, 141112 (2014).
23) T. Schupp, T. Meisch, B. Neuschl, M. Feneberg, K. Thonke, K. Lischka, and D. J. As, Phys. Status Solidi C **8**, 1495 (2011).
24) E. Peter, A. Dousse, P. Voisin, A. Lemaître, D. Martrou, A. Cavanna, J. Bloch, and P. Senellart, Appl. Phys. Lett. **91**, 151103 (2007).
25) S. L. McCall, A. F. J. Levi, R. E. Slusher, S. J. Pearton, and R. A. Logan, Appl. Phys. Lett. **60**, 289 (1992).
26) M. Borselli, T. J. Johnson, and O. Painter, Opt. Express **13**, 1515 (2005).
27) S. Sergent, S. Kako, M. Bürger, T. Schupp, D. J. As, and Y. Arakawa, Phys. Rev. B **90**, 235312 (2014).